We are IntechOpen,
the world's leading publisher of
Open Access books
Built by scientists, for scientists

4,800
Open access books available

122,000
International authors and editors

135M
Downloads

Our authors are among the

154
Countries delivered to

TOP 1%
most cited scientists

12.2%
Contributors from top 500 universities

CLARIVATE ANALYTICS
BOOK CITATION INDEX
INDEXED

WEB OF SCIENCE™

Selection of our books indexed in the Book Citation Index
in Web of Science™ Core Collection (BKCI)

Interested in publishing with us?
Contact book.department@intechopen.com

Numbers displayed above are based on latest data collected.
For more information visit www.intechopen.com

On FVM Transport Phenomena Prediction in Porous Media with Chemical/Biological Reactions or Solid-Liquid Phase Change

Nelson O. Moraga[1] and Carlos E. Zambra[2]
[1]Universidad de La Serena/Departamento de Ingeniería Mecánica, La Serena
[2]Centro de Investigación Avanzada en Recursos Hídricos y Sistemas Acuosos (CIDERH)
CONICYT-REGIONAL GORE-TARAPACÁ, Iquique
Chile

1. Introduction

The aim of the chapter is to show the FVM capabilities in the accurate and efficient prediction of transport phenomena in porous media including either biological, chemical reactions or liquid-solid phase transformations. Four applied technological problems are solved with the FVM. Problem 1 is related to heat and mass diffusion in a saturated porous media where chemical and biological reactions occur. Such a situation can be found in compost piles resulting from contaminated water treatments. Field experimental data are used to assess the quality of FVM calculations for temperature and oxygen concentration distribution time variations along the prediction of thermal explosions (Moraga, 2009) and effect of the moisture in compost piles self-heating (Zambra, 2011). Problem 2 deals with the improvement of thermal energy efficiency and pollution reduction in hydrocarbons combustion. Methane combustion with air in a cylindrical porous burner is investigated by solving 2D unsteady continuity, linear momentum, energy, and chemical species governing equations with the FVM. Sensibility studies performed via numerical tests allowed to obtain numerical results for unsteady velocity and temperature distributions, along to the displacement of the combustion zone. The effects of inlet reactants velocity (methane and air) in the range 0.3-0.6 m/s; excess air ratios between 3 and 6 and porosities of 0.3 up to 0.6 in the fluid dynamics, forced convection heat transfer and combustion process are described (Moraga, 2008). Problem 3 is devoted to characterize 3D natural convection and heat conduction with solidification inside a cavity filled with a porous media, in which a Darcy-Brinkman-Forchheimer flow model is used. This infiltration technique can be applied to produce new materials with enhanced physical properties. A fixed grid method is used along the FVM to solve, with a temperature dependent liquid fraction, the moving boundary problem by using a power law model for binary non Newtonian alloys (Moraga, 2010; Moraga, 2010). Problem 4 describes 3D turbulent convective heat transfer in a bioreactor, including the self-heating of the porous material due to chemical and biological reactions. FVM simulation based on a coupled heat mass transfer external forced convection model is used to assess the effects of reactor geometry, self- heating parameters, air flow and temperature in the bioreactor performance. The mathematical model includes the convective turbulent flow of momentum, energy and oxygen concentration, with

the κ-ε turbulence model, and the diffusion of energy and oxygen concentration in the saturated porous medium. Numerical results for the dependent variables are successfully validated with experimental data. Issues such as the use of dynamic time steps, under-relation of dependent variables and local refined meshes are discussed in each one of the problems solved. The pressure-velocity-temperature-chemical species coupling is discussed and a novel PSIMPLER method for the FVM is presented (Moraga, 2010). The stability, rate of convergence and efficiency of the PSIMPLER method is determined by solving natural, forced and mixed heat convection inside cavities by comparison with the solution obtained by using the standard SIMPLE algorithm. Improvements achieved in convergence rates by modifying the predictor-corrector schemes used to solve the discretized fluid mechanics, heat and mass transfer equations are discussed in some of the numerical experiments presented.

2. General scheme for the classic Finite Volume Method (Patankar, 1980)

Convective fluid dynamics/heat and mass transfer, for either laminar or turbulent flows of Newtonian or non-Newtonian fluids, with phase change in porous media is described by partial differential equations. Systems of nonlinear second order partial differential equations can be efficiently solved numerically using the finite volume method. Each governing equation is treated in the generalized form for a transport equation, with unsteady, convection, diffusion and linearized source terms:

$$\frac{\partial(\rho\phi)}{\partial t} + div(\rho\vec{u}\phi) = div(\Gamma \ grad\phi) + S_p\phi + S_c \tag{1}$$

where ϕ is the dependent variable, ρ density, t time, $\vec{u}$ velocity vector, Γ diffusion coefficient, S_c independent source term and S_p dependent source term. No convection is considered inside the volume occupied by the MWM, since the flow velocities are zero in that region, and diffusion becomes the only transport mechanism inside this porous medium. This "blocked" region is implemented by setting a very large numerical viscosity (10^{30}) for the control volumes enclosed in such region, which renders the velocity essentially zero ($\sim 10^{-30}$) inside the material.

The time integration is performed with an explicit Euler scheme:

$$\frac{\partial\phi}{\partial t} = \frac{\phi^{t+\Delta t} - \phi^t}{\Delta t} \tag{2}$$

At each time step, the system of discretized nodal equations for each main dependent variable (velocity components, temperature and mass fraction) is solved iteratively by internal iterations, with a combination of the alternating tri-diagonal matrix algorithm (TDMA) and Gauss-Seidel method. The sequential coupling of these main variables is accomplished by the SIMPLE method in the external iterations. Under-relaxation is always applied to the dependent variables during these external iterations.

3. Self-heating in compost pile solved with FVM

3.1 General mathematical models for porous media applied to compost pile

Richard equation (RE) (Richards, 1931) is a standard, frequently used approach for modeling and describing flow in variably saturated porous media. When do not consider

gravitational and the source term effects, and is introduced a new term $D_{(\theta)}$, the follow equation can be used:

$$\frac{\partial \theta}{\partial t} = \nabla D_{(\theta)} \nabla \theta \tag{3}$$

The volumetric water content θ is the quotient between water volume and the total sample volume, so it is has not unit and its values are between 0 and 1.

The effects of the porosity and type of soil should be introduced by the $D_{(\theta)}$ parameter. A non-linear equation for this parameter is reported for Serrano (Serrano, 2004).

$$D_{(\theta)} = \upsilon_1 e^{\lambda(\theta)^{\alpha}} - \upsilon_2 \tag{4}$$

The constants $\upsilon_1, \upsilon_2, \lambda$ and α, may be obtained by experimental field test. The Eqs. (3) and (4) are used when the specific hydraulic properties of the compost pile are not available. Oxidation and microorganism activity inside the pile are incorporated in the model by volumetric heat generation. For simplicity, local thermal equilibrium is assumed, which is a common assumption for porous medium and packed particle beds (Nield & Bejan, 1992). The equations for the temperature and the oxygen concentration are (Zambra et al., 2011):

$$\frac{\partial \left(\rho C_{p,T} \right)_{eff} T}{\partial t} = \nabla K_{eff} \nabla T + Q_c \varepsilon_s A_c^* \rho_c C_{ox} e^{\left(\frac{-E_c}{RT} \right)} + Q_b \varepsilon_s \rho_b \rho_c \frac{A_1^* e^{\left(\frac{-E_1}{RT} \right)}}{1 + A_2 e^{\left(\frac{-E_2}{RT} \right)}} - L_v \rho_{va} q(\theta) X_v \tag{5}$$

$$\varepsilon_{air} \frac{\partial C_{ox}}{\partial t} = \nabla D_{eff} \nabla C_{ox} + \varepsilon_s A_c^* \rho_c C_{ox} e^{\left(\frac{-E_c}{RT} \right)} \tag{6}$$

In Eqs. (5) and (6) $A_1^* = A_1 * \upsilon_1$ and $A_c^* = A_c * \upsilon_c$, where A_1 and A_c are the pre-exponential factor for the oxidation of the cellulose and bio-mass growth, respectively. The coefficients υ_1 and υ_c are parameters that allows relations between the variables T and C_{ox} which are function of the moisture and oxygen concentration at time t. The constants E_c, E_1, E_2, are the activation energy for the cellulose, bio-mass growth and inhibition of biomass growth, respectively. The effects of the vaporization of water in the internal energyare calculated with the third term of the right hand side of Eq. (5), where L_v is the vaporization enthalpy, ρ_{va} is the water vapor density, $q(\theta)$ is the mass water flux and X_v is the vapor quality. The total porosity (ε_{fl}) is calculated in terms of the apparent density and real density, ε_w and ε_{air} are the fraction of water and air into the pore respectively.

$$\varepsilon_{fl} = \frac{\rho_{real} - \rho_{app}}{\rho_{app}}; \qquad \varepsilon_{fl} = \varepsilon_w + \varepsilon_{air}; \qquad 1 - \varepsilon_{fl} = \varepsilon_s \tag{7}$$

Thermodynamics equilibrium and ideal mixture between oxygen and water are assumed in the porous medium,

$$K_{eff} = \varepsilon_{air}k_{air} + \varepsilon_w k_w + \varepsilon_s k_c \tag{8}$$

$$\left(\rho C_{p,T}\right)_{eff} = \varepsilon_{air}\rho_{air}C_{p,air} + \varepsilon_w\rho_w C_{p,w} + \varepsilon_s\rho_c C_{p,c} \tag{9}$$

$$D_{eff} = \varepsilon_{air}D_{air,c} \tag{10}$$

where K_{eff} and D_{eff} are the effective properties which are considered dependent of temperature, and $C_{p,air}$, $C_{p,w}$ and $C_{p,c}$ are specific heat capacity of the air, water and cellulose. Oxygen concentrations variations are affected by cellulosic oxidation. This assumption is incorporated in the second term of right hand side Eq. (6).

3.2 Diffusion of temperature and oxygen concentration

3.2.1 Mathematical model

Cellulosic oxidation and micro-organism activity inside the compost pile are taken into account by the model in the form of a volumetric heat generation source. When is considered one fluid phase (air), the heat transfer eq. (5) take the form.

$$\left(\rho C_{p,T}\right)_{eff}\frac{\partial T}{\partial t} = K_{eff}\nabla^2 T + Q_c(1-\varepsilon)A_c\rho_c C_{ox}e^{\left(\frac{-E_c}{RT}\right)} + Q_b(1-\varepsilon)\rho_b\rho_c\frac{A_1 e^{\left(\frac{-E_1}{RT}\right)}}{1 + A_2 e^{\left(\frac{-E_2}{RT}\right)}} \tag{11}$$

while the oxygen concentration within the pile is described by

$$\varepsilon_{air}\frac{\partial C_{ox}}{\partial t} = D_{eff}\nabla^2 C_{ox} + (1-\varepsilon)A_c\rho_c C_{ox}e^{\left(\frac{-E_c}{RT}\right)} \tag{12}$$

In equations (3) and (4), A_c is the pre-exponential factor for the oxidation rate of the cellulose, and. Heat and mass transfer properties in the porous medium are defined in terms of the pile porosity ε as

$$K_{eff} = \varepsilon_{fl}k_{air} + (1-\varepsilon_{fl})k_c \; ; \quad \left(\rho C_{p,T}\right)_{eff} = \varepsilon_{fl}\rho_{air}C_{p,air} + (1-\varepsilon_{fl})\rho_c C_{p,c} \; ; \quad D_{eff} = \varepsilon_{fl}D_{air,c} \tag{13}$$

where K_{eff} and D_{eff} are respectively the effective thermal conductivity and diffusion coefficient, which are considered independent of the temperature and concentration. In these expressions the subscript c refers to the cellulose. Details for the formulation of the term representing the heat generated by the biomass have been given by Chen and Mitchell (Chen & Mitchell, 1996). The parameter values used in the mathematical model for the processes that take place inside the porous block of waste material were obtained from reference (Sidhu et al., 2007) and are presented in Table 1.

Parameter	Value	Parameter	Value
A_C	1.8×10^4	$C_{ox,0}$	0.272
A_1	2×10^6	Q_b	7.66×10^6
A_2	6.86×10^{32}	Q_C	5.5×10^9
C_{air}	1005	k_{air}	0.026
C_C	3320	k_C	0.18
$D_{o,air}$	2.4×10^{-7}	ε_{fl}	0.3
E_C	1.1×10^5	ρ_{air}	1.17
E_1	1×10^5	ρ_b	575
E_2	2×10^5	ρ_c	1150

Table 1.Constant values used in the mathematical model for the internal processes in the compost pile.

3.2.2 Numerical results of temperature time evolution and grid study

A 2D case of self-heating in a rectangular porous pile, with 2.5 m height (H) and 5 m length (L), was investigated using three grids, with 100x100, 200x200 and 300x300 nodes, and three time steps: 300s, 600s and 3600s.The temperature time evolution was calculated in the three positions: f) H/4, L/4; g) H/2, L/2 and h) 3H/4, 3L/4.Results of the time needed to cause auto-ignition, in days, are shown in Table 2, for the three positions. The use of a time step of 600s and a grid with 300x300 nodes allows to calculate a time for auto-ignition: 247, 246 and 250 days, at the three vertical positions, respectively, independently of the time a space discretizations, as is showed in the table 2.

Grids	Δt (s)	f) H/4,L/4	g) H/2,L/2	h) 3H/4, 3L/4
100x100	3600	247	245	249
	600	248	248	250
	300	244	241	246
200x200	3600	248	246	251
	600	250	249	253
	300	246	244	249
300x300	3600	248	247	252
	600	247	246	250
	300	247	246	250

Table 2.Days before the self-ignition in positions f), g) and h) within the compost pile.

Fig. 1 shows the time evolution results of temperature in the f) position: H/4, L/4, calculated with a grid of 300x300 nodes using two time steps: 300s and 3600s. A typical heating curve for the temperature is observed in the Figure 1a. Auto-ignition at H/4, L/4 occurs after 247 days. The temperature increased suddenly in one day from 370 to 515K. A complex system of solid, liquid and gaseous fuels as a final result of the cellulosic oxidation originated a volumetric heat generation causing the self-ignition process. Temperature

decreasing in time, characterized the last stage, in which the fuel reserves in the location are exhausting. Figure 1b, a zoom view of Fig. 3a for the time interval between days 240 and 255, shows that a time step reduction from 3600s to 300s allows to determine a more accurate prediction (within 1 day) for the time needed to insatiate the self-ignition in a 2.5m height compost pile. Due to the previous analysis, a mesh with 300x300 nodes and a dynamic time step with 300s during the auto-ignition and 3600s in other states may be used in the calculation of the processes of self-heating with thermal explosion.
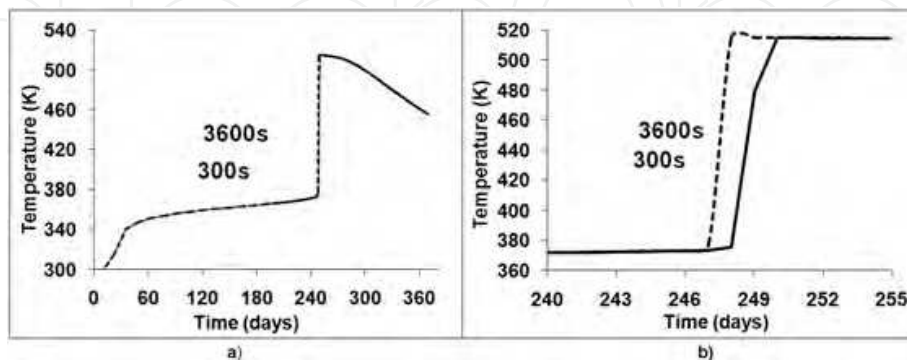
Fig. 1. Temperature evolution calculated with two time steps, 300x300 mesh, at position H/4, L/4, for a 2.5 m high pile, a) full time scale, b) during thermal explosion.

3.2.3 Comparison between experimental and numerical results.

The experimental data and numerical results in 2D obtained with the FVM for a 2.5 m high pile and trapezoidal form, are compared in Figure 2. Data obtained from numerical calculations were plotted considering daily output at 12:00 AM. The experimental and predicted data follow the same general trends. Near the surface (0.35 m depth) during the third week the main differences found are not larger than 3 °C. The best description of the experimental data was obtained at a depth of 2.1 m.
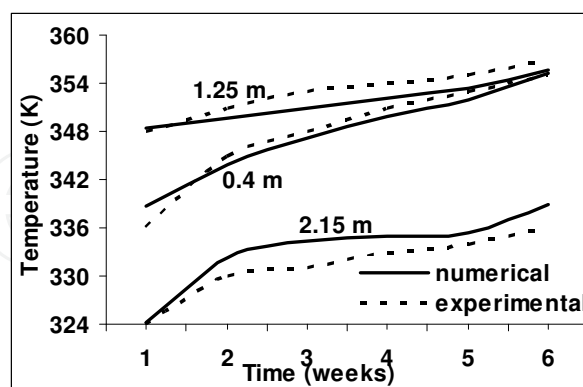

Fig. 2. Comparison between experimental and numerical temperature values during six weeks.

3.3 Inhibition of the self-ignition in the sewage sludge waste water treatment

The coupled heat and mass diffusion equations system of partial differential equation (11)-(15), is solved in 3D by the finite volume method. In previous works Moraga et al. (Moraga

et al., 2009) established that statics compost pile with high less than 1.5 m do not have self-ignition. Other statics compost pile higher than 1.5 m may have self-ignition. This restriction decreases the possibilities of the storage in field of this material. Moraga and Zambra (Moraga and Zambra, 2008) proposed a novel method for the inhibition of the self-ignition in large piles. A uniform mesh with 94x32x62 nodes in x, y and z directions was found to be adequate by comparison of results between plane 2D and the central plane 3D (x and y directions) in a trapezoidal pile. Figure 3 compares the numerical results 2D and 3D in three positions inside the pile. The small differences of the values are produced for the third dimension incorporated in the simulations. The main differences in the temperature values occur when the self-ignition reached the tested position.
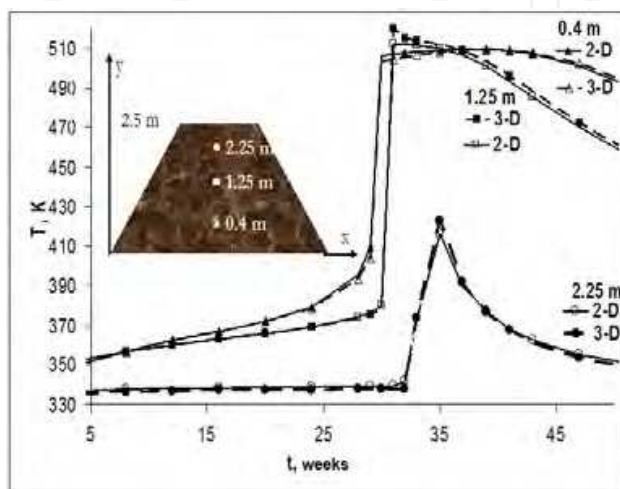
Fig. 3. Comparison of numerical results of temperature for a trapezoidal plane 2D and central plane 3D.

In figure 4 the physical situation used for the inhibition of the ignition is shown.
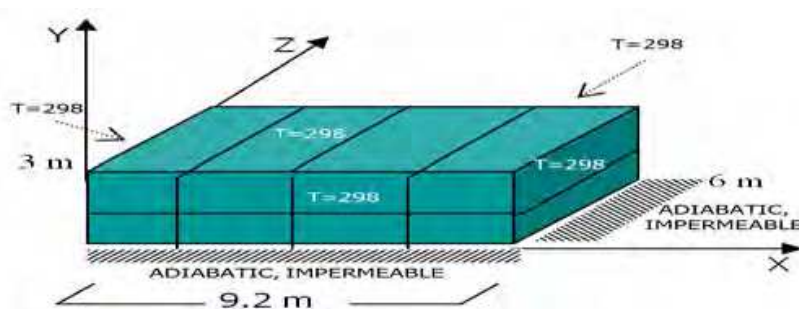

Fig. 4. Three-dimensional physical situation used for a large pile.

A parallelepiped of 9.2 m, 3 m and 6 m in x, y and z directions respectively, was used. Insulation and impermeable walls was introduced to regular interval in vertical and horizontal directions within the pile. The pile base is adiabatic and impermeable to the oxygen diffusion. A temperature of 298 K, was imposed at the border. Initially, the temperature and oxygen concentration inside the pile is constant. Perpendicular steel walls with thick 0.1 m and each 2.225 m to separate the pile in 8 sections to the long of the x coordinate were used. The table 1 shows the parameters used in the mathematical model. Numerical results of maximum values for the temperatures and oxygen concentrations are

presented in figure 5. Clearly the self-ignition not occurs. The steel walls allow the inhibition of the thermal explosion because the oxygen diffusion within the pile is restricted. The maximum temperatures and minimum oxygen concentration reaches the 355 K and 0.262 kg/m^3, respectively.
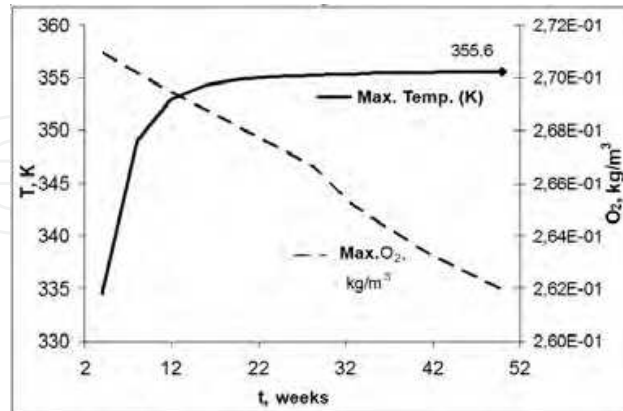

Fig. 5. Maximum values of the temperatures and oxygen concentrations for the sectioned pile.

Distribution of the temperature and the oxygen concentrations in a central plane of the sectioned pile are presented in figure 6. The walls do not allows the oxygen diffusion and the below sections have similar behavior to the 1.5 m high single pile. The temperature isconduced trough the walls but do not have influence in the self-ignition of the neighbor section.
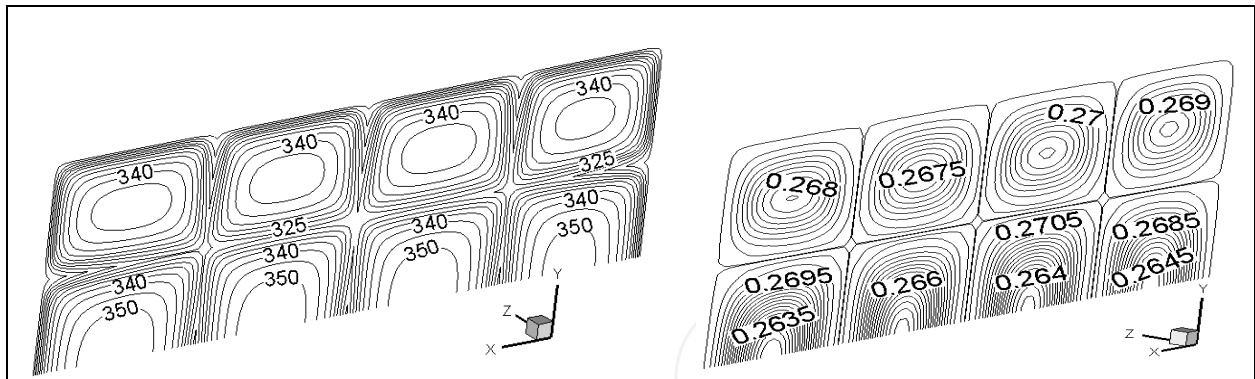

Fig. 6. Temperature and oxygen distribution within of the sectioned pile.

4. Combustion and convective heat transfer in porous medium combustors

4.1 Numerical simulation of a cylindrical porous medium burner

A porous media combustor, built on base of alumina spheres placed inside of an axi-symmetric cylindrical quartz tube of 0.52 m in length and 0.076 m in diameter, is shown in Fig. 7. Methane and air mixture enter to the combustor at ambient temperature with uniform velocity. To start the combustion a temperature profile of one step type, with a maximum temperature of 1150 K and a thickness of 4 cm is assumed to simulate the ignition by means of an external energy source. In the combustion zone, the products: CO_2, H_2O, O_2 and N_2 are generated. Air, gas and products are assumed to behave as ideal gases and hence

density is calculated in terms of temperature from the ideal gas state equation. Burners based on this technology has been investigated and tested for many industrial applications (Foutko et al., 1996, Zhdanok et al., 1995).
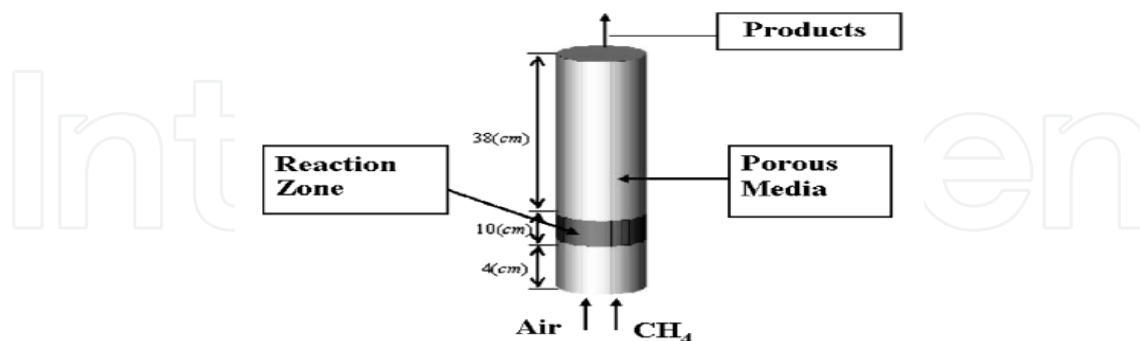

Fig. 7. Porous media combustor.

The assumptions used to build the mathematical model include: single-step chemical reaction, laminar 2D flow of Newtonian fluid of ideal gases. The mathematical model includes the porosity terms in both the energy equations for the solid as well as for the gas; similarly, also the continuity, linear momentum and fuel mass fraction equations are included. All physical properties are variable with temperature, and it is postulated that density varies according to the ideal gases state equation. The chemical reaction for methane is considered to be in a single step, with excess air included.

$$CH_4 + 2(1+\psi)(O_2 + 3.76N_2) \rightarrow CO_2 + 2 \cdot H_2O + 2\psi \cdot O_2 + 7.52(1+\psi)N_2 \tag{14}$$
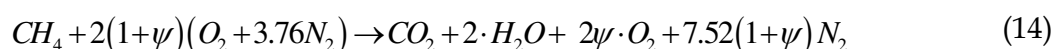
Continuity and ideal gas equations

$$\frac{\partial(\rho \cdot v_r)}{\partial r} + \frac{\rho \cdot v_r}{r} + \frac{\partial(\rho \cdot v_z)}{\partial z} = 0; \quad \rho = \frac{\rho_0 \cdot T_0}{T} \tag{15}$$

Linear momentum in radial r and axial z directions:

$$\frac{\partial(\rho \cdot v_r)}{\partial t} + v_r \frac{\partial(\rho \cdot v_r)}{\partial r} + v_z \frac{\partial(\rho \cdot v_r)}{\partial z} = -\frac{\partial p}{\partial r} + \frac{\partial^2(\mu \cdot v_r)}{\partial r^2} + \frac{1}{r}\frac{\partial(\mu \cdot v_r)}{\partial r} - \frac{\mu \cdot v}{r^2} + \frac{\partial^2(\mu \cdot v_r)}{\partial z^2} \tag{16}$$

$$\frac{\partial(\rho \cdot v_z)}{\partial t} + v_r \frac{\partial(\rho \cdot v_z)}{\partial r} + v_z \frac{\partial(\rho \cdot v_z)}{\partial z} = -\frac{\partial p}{\partial z} + \frac{\partial^2(\mu \cdot v_z)}{\partial r^2} + \frac{1}{r}\frac{\partial(\mu \cdot v_z)}{\partial r} + \frac{\partial^2(\mu \cdot v_z)}{\partial z^2} \tag{17}$$

Fuel mass conservation equation

$$\frac{\partial(\rho \cdot w)}{\partial t} + v_r \frac{\partial(\rho \cdot w)}{\partial r} + v_z \frac{\partial(\rho \cdot w)}{\partial z} = \frac{\partial}{\partial r}\left(D^M \cdot \rho \cdot \frac{\partial w}{\partial r}\right) + \frac{\partial}{\partial z}\left(D^M \cdot \rho \cdot \frac{\partial w}{\partial z}\right) - \rho \cdot K \cdot w \cdot e^{\frac{-Ea}{Ro \cdot T}} \tag{18}$$

Two energy equations were used for gas and solid in the porous medium

$$\varepsilon \cdot \left(\frac{\partial(\rho \cdot Cp \cdot T)}{\partial t} + v_r \frac{\partial(\rho \cdot Cp \cdot T)}{\partial r} + v_z \frac{\partial(\rho \cdot Cp \cdot T)}{\partial z}\right) = -\alpha(T_G - T_S) - \varepsilon \cdot \rho \cdot \Delta h \cdot K \cdot w \cdot e^{\frac{-Ea}{Ro \cdot T}} \tag{19}$$

$$(1-\varepsilon)\cdot\left(\frac{\partial(\rho_s\cdot Cp_s\cdot T_s)}{\partial t}\right)=\frac{1}{r}\frac{\partial}{\partial r}\left(r\cdot\lambda_{eff}\frac{\partial T_s}{\partial r}\right)+\frac{\partial}{\partial z}\left(\lambda_{eff}\frac{\partial T_s}{\partial z}\right)+\alpha\left(T_G-T_s\right) \tag{20}$$

where the chemical reaction speed and the effective conductivity of the solid including radiation are:

$$r_f=w_i\cdot\rho_G\cdot K\cdot\exp\left(-\frac{Ea}{Ro\cdot T}\right)\quad \lambda_{eff}=(1-\varepsilon)\lambda_s+\frac{32\cdot\sigma\cdot\varepsilon\cdot dp\cdot T_s^3}{9\cdot(1-\varepsilon)} \tag{21}$$

The coefficient of convective heat transfer between solid and gas is calculated as follows

$$\alpha=\frac{6(1-\varepsilon)}{dp}\cdot\frac{\lambda_G}{dp}\cdot Nu\,;\quad Nu=2.0+1.1\cdot\left(\mathrm{Pr}^{1/3}\cdot\mathrm{Re}^{0.6}\right)\,;\ \mathrm{Re}=\frac{\varepsilon\cdot u\cdot dp\cdot\rho}{\mu} \tag{22}$$

Conjugate boundary conditions between the porous burner section and the annular one are used in the internal and external areas of the inner tube:

$$T_i(r_i,z,t)=T_t(r_i,z,t);\ -\lambda_{eff}\frac{\partial T_i}{\partial r}=-\lambda_t\frac{\partial T_t}{\partial r}\,;\ T_t(r_e,z,t)=T_e(r_e,z,t)\,;\ -\lambda_t\frac{\partial T_t}{\partial r}=-\lambda_a\frac{\partial T_a}{\partial r} \tag{23}$$

The parameters used in the simulation included the Stephan–Boltzmann constant (σ), combustion enthalpy (Δh_{COMB}), frequency factor (K), activation energy (E_a), and the universal gas constant (Ro), whose respective values are: $\sigma=5.67\cdot10^8\,W/m^2K^4$; $\Delta h_{COMB}=50.15\cdot10^6\,J/kg$; $K=2.6\cdot10^8(1/s)$ and $Ea/Ro=15643.8K$. The mass diffusion coefficient was found by assuming that the Lewis number was equal to 1,

$$D^M=\frac{\lambda_G}{(\rho\cdot Cp)_G}\,;\quad (Le=1)\,;\quad \lambda_G=\frac{\mu\cdot Cp}{\mathrm{Pr}}\,;\ D^M=\frac{\mu}{\rho\cdot\mathrm{Pr}} \tag{24}$$

Inlet and outlet boundary conditions of the heat exchanger are:

$$Z=0.0,\quad when\ \begin{cases}0\le r\le0.038 & \Rightarrow U_0=0.43\wedge T=300K\\[4pt]0.038\le r\le0.077 & \Rightarrow \dfrac{\partial u}{\partial z}=\dfrac{\partial T}{\partial z}=0\end{cases}$$
$$Z=1.5,\quad when\ \begin{cases}0\le r\le0.038 & \Rightarrow U_0=0.43\wedge T=300K\\[4pt]0.038\le r\le0.077 & \Rightarrow U_0=\dfrac{\mathrm{Re}\cdot v}{D_h}\wedge T=283K\end{cases} \tag{25}$$

4.1.1 Solution procedure

The coupled, strongly non-linear system of partial differential equations was solved numerically using the FVM, with the SIMPLE algorithm (Patankar, 1980). A fifth power law was used to calculate the convective terms while the diffusion terms were determinated by linear interpolation functions for the dependent variables between the nodes. Each one of the governing equations was written in the general form of the transport equation, with unsteady, convective, diffusion and linearized source terms:

$$\frac{\partial(\rho\cdot\phi)}{\partial t}+div(\rho\cdot\vec{v}\cdot\phi)=div(\Gamma\cdot grad\,\phi)+Sc+Sp\cdot\phi \tag{26}$$

The convergence criteria used for gas and solid temperature, fuel mass fraction and for the two velocity components were

$$\left| \phi_{i,j}^k - \phi_{i,j}^{k-1} \right| \leq 10^{-3}, \text{ for } T_G, T_S, w_i; \quad \text{and} \quad \left| \phi_{i,j}^k - \phi_{i,j}^{k-1} \right| \leq 10^{-4}, \text{ for } \boldsymbol{u} \text{ and } \boldsymbol{v} \tag{27}$$

A non-uniform grid with 622 x 15 nodes, in axial and radial directions, respectively, was found by a trial and error procedure to be efficient to solve the discretized model with accuracy and a reasonable computation time (Moraga et al., 2008). The iterative solution procedure was based on the use of the line by line method,that combines the TDMA algorithm with the under-relaxed Gauss-Seidel algorithm. The under-relaxation coefficients used were equal to 0.1, for velocity components, and 0.5, for gas and solid temperatures and for the fuel ratio. A strategy based on a dynamic time step was implemented to calculate the unsteady terms. The initial time step used in the calculation procedure was equal to 0.00001s until t = 0.001s, and then was increased by and order of magnitude as time increased one order of magnitude, to end up with a time step equal to 0.1s when time was over 0.1s.

4.1.2 Results and discussion

Numerical experiments were performed to assess the effect of porosity, inlet gas velocity and excess air coefficient on the fluid dynamics and heat transfer in the porous media burner. The effect of increasing porosity from 0.3 to 0.6 on the axial velocity at four axial locations is shown in figure 8a, while the influence of the inlet velocity is depicted in figure 8b. The increments of porosity causes a reduction in axial velocity and in the velocity gradients near the walls. Axial velocity increases with time and a maximum value is reached for $\varepsilon = 0.3$, when t = 600s, at 0.15m from the inlet. Secondary flows are observed near the wall (z = 0.21m) when $\varepsilon = 0.3$. The axial velocity profile increases with time, when the initial velocity Uo = 0.3m/s, reaching a maximum at 900s, at z= 0.15m and up to 1500s for z = 0.21m.

Superadiabatic combustion in the porous media combustor causes temperature increments from 300 K, near the inlet and close to the oulet, to 1600 K in the flame region, as depicted in figure 9. A displacement of the combustion front toward the middle of the combuster is achieved by increasing the air excess ratio ψ from 3.0 to 6.0. Similar effects in the temperature distribution can be noticed when porosity increased from $\varepsilon = 0.3$ to $\varepsilon = 0.6$ and when the inlet velocity increased from Uo = 0.3 m/s to Uo = 0.3 m/s. The displacement of the combustion zone, typical for porous combustor with uniform porosity and cross section, in the direction of the burner exit has been shown to be strongly influenced by increments in the values of: excess air ratio, porosity and inlet reactants velocity. The porous combustor design requires a reduced combustion front displacement. The results obtained (table 2) show that the displacement velocity of the combustion front decreases when the porosity and inlet reactants are reduced, and when the excess air ratio increases.Table 3 shows that a change in the mathematical model, from 1D to 2D, caused increments of about 5% in the gas temperature, 7% in the solid temperature and up to 3% in the combustion front velocity.

Figure 10 shows that main changes caused by the radial diffision of heat, captured with the 2D model, are larger after the combustion zone, where higher temperature are obtained.
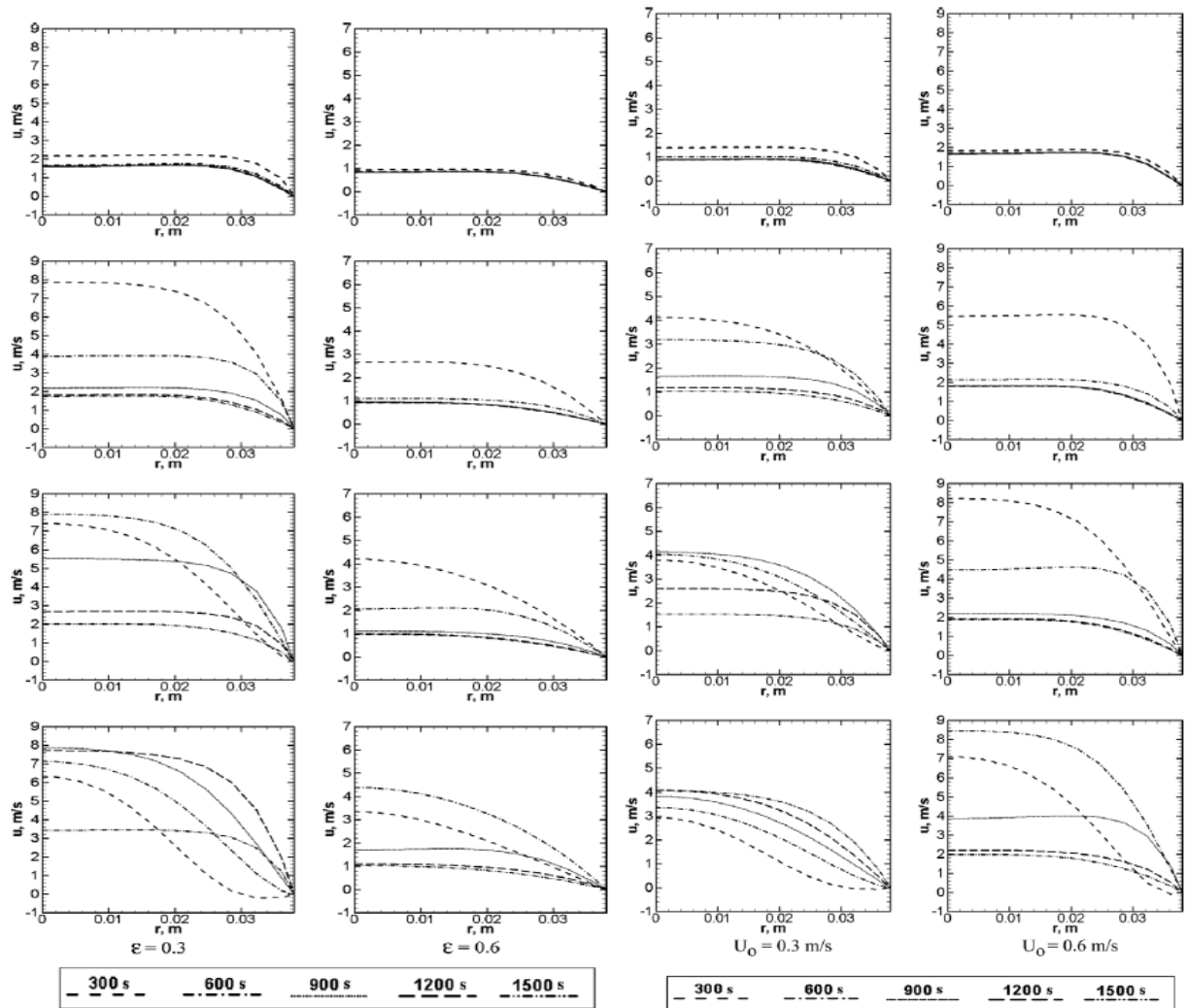
a) Effects of porosity. U_o= 0.43 m/s, ψ= 4.88   b) Effects of inlet velocity. ψ= 4.88, ε= 0.4

Fig. 8. Effects of porosity and inlet velocity on axial velocity along the burner. Axial locations (from top to bottom): 0.05m, 0.10m, 0.15m and 0.21m.
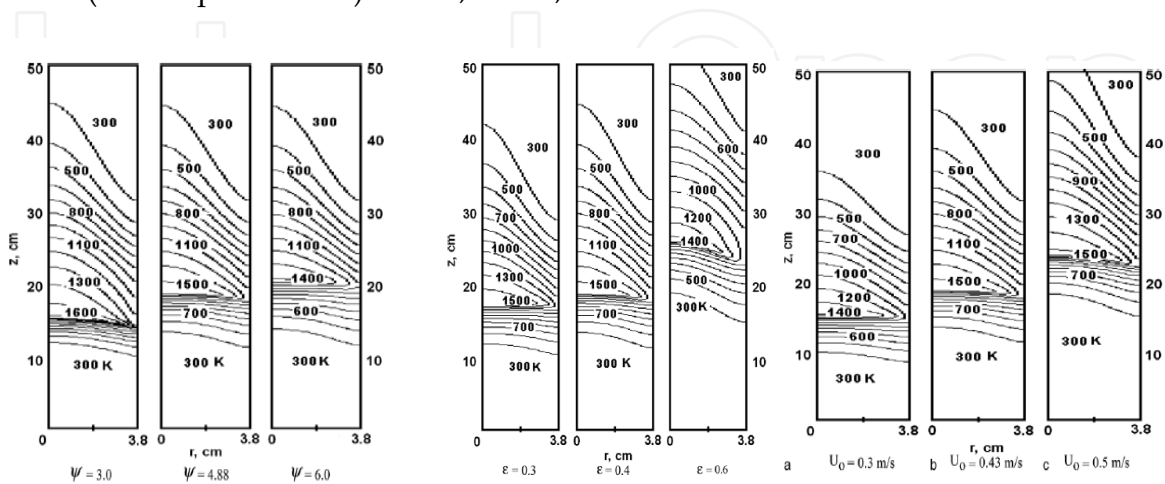

Fig. 9. Effects of excess air (left), porosity (center) and inlet velocity wright) on gas temperature at time t = 15 min.

Excess of air	Porosity	v_{in}(m/s)	Model	Gas T_{max} (K)	Solid T_{max} (K)	Combustion front velocity (m/s)
3.00	0.4	0.43	1D	1569.87(4.50%)	1417.39(7.06%)	9.538E-05(1.74%)
			2D	1640.45	1517.47	9.417E-05
4.88	0.4	0.43	1D	1404.44(4.99%)	1323.31(6.85%)	1.250E-04(0.67%)
			2D	1474.57	1413.95	1.258E-04
4.88	0.3	0.43	1D	1424.87(4.99%)	1354.25(6.98%)	1.108E-04(1.50%)
			2D	1496.03	1448.81	1.092E-04
4.88	0.6	0.43	1D	1368.51(5.03%)	1258.09(6.29%)	1.858E-04(2.69%)
			2D	1437.38	1337.18	1.908E-04
4.88	0.4	0.30	1D	1333.79(5.82%)	1246.03(7.32%)	9.167E-05(2.73%)
			2D	1411.39	1337.21	8.917E-05
4.88	0.4	0.60	1D	1465.13(3.53%)	1394.07(1.98%)	1.750E-04(0.48%)
			2D	1513.48	1421.52	1.758E-04

Table 3. Comparison between results of 1D and 2D models for porous media burner.
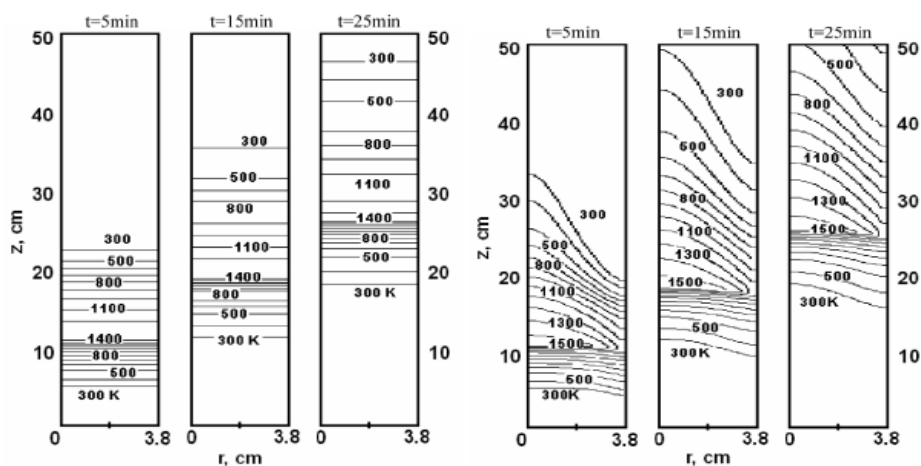

Fig. 10. Temperature distribution calculated with a 1D model (left side) and with a 2D model (right side)

4.2 Wood stove with porous medium post-combustor

4.2.1 Physical situation and mathematical model

The design of a porous post-combustor for a wood stove is investigated with FVM in order to reduce emissions. Figure 11 shows the post-combustor location in the gas exhaust tube along with some of the boundary conditions used in the analyis.Primary air inlet is located in the lower section of the stove front, secondary air enters in the upper section of the lateral walls through a three ways valve that allows high, medium or low secondary air injection and a terciary air inlet located in the upper section on the back, that allows for pre-heating of the auxiliary air.
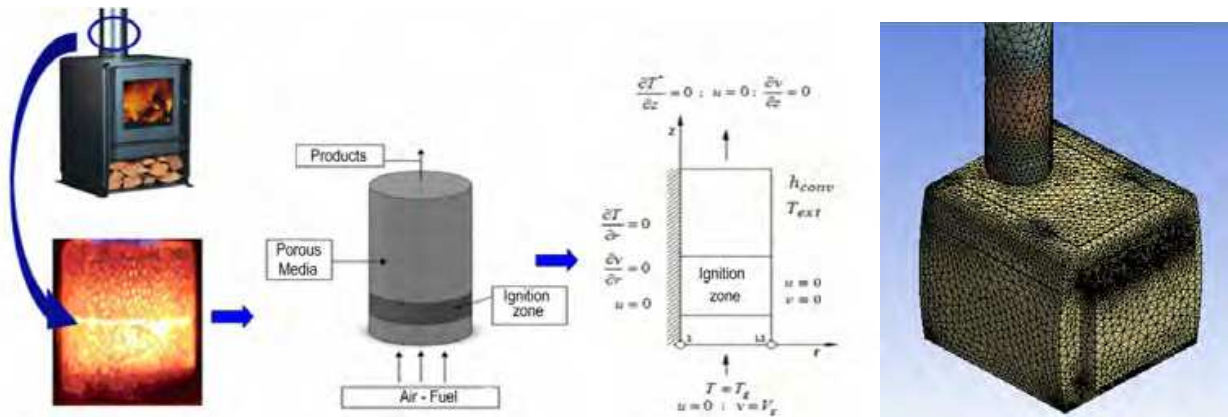
Fig. 11. Wood stove with a porous post combustor and mesh used in the FVM simulation.

The alumina porous combustor with a length of 300mm and a diameter of 150mm, was designed with two sections with different porous diameter of 1.52mm (length equal to 100mm) and 5.6 mm (with a length of 200mmm). An ignition temperature of 1150K was assumed in the simulations.

4.2.2 Solution procedure

A two stages procedure was used in the numerical study. In the first stage, a 3D turbulent k-e model was used to describe, with ANSYS/Fluent, the fluid mechanics and the convective heat transfer in the stove. Temperature and velocity distributions at the entrance of the exhaust stove pipe were found from the 3D model. Then, in the second stage, a secondary combustion process was described from a 2D laminar forced convection model in the porous post-combustor.

a. 3D k-e model for the turbulent gas flow inside the stove: Continuity, ideal gas, linear momentum, energy, species transport, turbulent kinetic energy and rate of dissipation equations:

$$\frac{\partial\left(\rho v_j\right)}{\partial x_j}=0 \; ; \quad \rho = \frac{\rho_0 T_0}{T} \tag{28}$$

$$\frac{\partial}{\partial x_j}\left(\rho v_j v_i\right)=-\frac{\partial p}{\partial x_i}+\frac{\partial}{\partial x_j}\left(\left(\mu+\mu_t\right)\frac{\partial v_i}{\partial x_j}\right)+\frac{\partial}{\partial x_j}\left(\left(\mu+\mu_t\right)\frac{\partial v_j}{\partial x_i}\right)+\rho g_i \tag{29}$$

$$\frac{\partial}{\partial x_j}\left(\rho v_j T\right)=\frac{\partial}{\partial x_j}\left(\lambda_{eff}\frac{\partial T}{\partial x_j}\right)+S_C \; ; \quad \lambda_{eff}=\lambda+\frac{c_P \mu_t}{\mathrm{Pr}_t}; \quad \mathrm{Pr}_t=0.85 \tag{30}$$

$$\frac{\partial}{\partial x_j}\left(\rho v_j Y_{m'}\right)=\frac{\partial}{\partial x_j}\left(\left(D_{m'}^M \rho+\frac{\mu_t}{Sc_t}\right)\frac{\partial Y_{m'}}{\partial x_j}\right)+S_{m'}; \quad Sc_t=0.7 \tag{31}$$

$$\frac{\partial}{\partial x_i}\left(\rho k v_i\right)=\frac{\partial}{\partial x_j}\left[\left(\mu+\frac{\mu_t}{\sigma_k}\right)\frac{\partial k}{\partial x_j}\right]+G_k+G_b-\rho\varepsilon \; ; \quad \mu_t=\rho C_\mu \frac{k^2}{\varepsilon} \tag{32}$$

$$\frac{\partial}{\partial x_i}\left(\rho\varepsilon v_i\right) = \frac{\partial}{\partial x_j}\left[\left(\mu + \frac{\mu_t}{\sigma_\varepsilon}\right)\frac{\partial\varepsilon}{\partial x_j}\right] + C_1\frac{\varepsilon}{k}\left(G_k + C_3 G_b\right) - C_2\rho\frac{\varepsilon^2}{k}$$ (33)

$$G_k = \mu_t\left[\frac{\partial v_i}{\partial x_j} + \frac{\partial v_j}{\partial x_i}\right]\frac{\partial v_i}{\partial x_j} \quad ; \quad G_b = \beta g_i\frac{\mu_t}{\Pr_t}\frac{\partial T}{\partial x_i}; \quad \beta = -\frac{1}{\rho}\frac{\partial\rho}{\partial T}$$ (34)

The values for the five constants used in the k-e turbulence model are those suggested by Launder and Spalding, 1974.

$$C_1 = 1.44; \quad C_2 = 1.92; \quad C_3 = 1.0; \quad C_\mu = 0.09; \quad \sigma_k = 1.0; \quad \sigma_\varepsilon = 1.3$$ (35)

b. 2D Darcy-Brikman-Forcheimer model for the laminar gas flow in the porous media post-combustor: Continuity, ideal gas, linear momentum, energy and species transport equations

$$\frac{\partial\left(\rho v_j\right)}{\partial x_j} = 0 \quad ; \quad \rho = \frac{\rho_0 T_0}{T}$$ (36)

$$\frac{\partial}{\partial x_j}\left(\rho v_j v_i\right) = -\frac{\partial p}{\partial x_i} + \frac{\partial}{\partial x_j}\left(\mu\frac{\partial v_i}{\partial x_j}\right) - \rho g_i - \left(\frac{\mu}{\alpha} + \frac{C|\vec{V}|}{\sqrt{\alpha}}\right)v_i; \quad C = 0.55$$ (37)

$$\frac{\partial}{\partial x_j}\left(\rho v_j T\right) = \frac{\partial}{\partial x_j}\left(\lambda_{ef}\frac{\partial T}{\partial x_j}\right) \quad ; \quad \lambda_{ef} = \gamma\lambda_f + \left(1-\gamma\right)\lambda_s$$ (38)

$$C_P\frac{\partial}{\partial x_j}\left(\rho v_j Y_{m'}\right) = \frac{\partial}{\partial x_j}\left(D_{m'}^M\rho\frac{\partial Y_{m'}}{\partial x_j}\right)$$ (39)

The air flow for the three operational modes inside the stove combustion chamber is shown in figure 12.
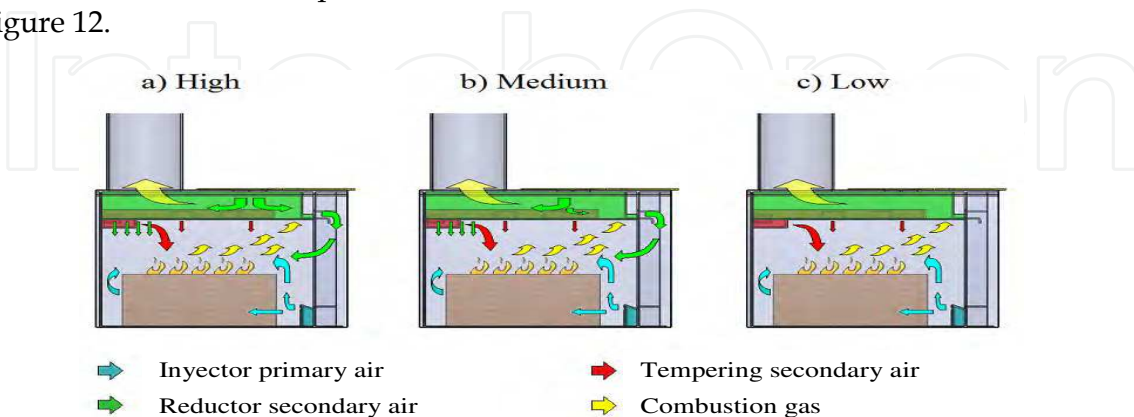

Fig. 12. Air flow inside the primary combustor chamber for the three operacional modes.

The 3D model for the combustion zone of the stove was discretised with 736,767 tethahedral, 18,032 wedge and 280 pyramidal elements. Under-relaxation coefficients for

pressure were: 0.2 for pressure, 0.3 for the three velocity components, 0.7 for the kinetic energy and for the dissipation rate of the kinetic energy and 0.9 for temperature. Axial discretization for the 2D porous postcombustor included 40 nodes in the pre-heating section, from z = 0 to z = 2cm, 450 nodes in the flame region, up to z= 24cm, 100 nodes in the post-secondary combustion zone (from z=24 to z=30cm) and 30 nodes in the last zone (from z= 30cm to z= 60cm in z direction). The convergence was assumed when the maximum deviation for each dependent variable, at each control volume and for all time steps, $\Phi^k_{i,j}-\Phi^{k-1}_{i,j}$ was smaller than 0.0001 for the velocity components and smaller than 0.001 for solid and gas temperature. Under-relaxation factors were equal to 0.1 for the velocity components, 0.5 for gas and solid temperature and equal to 0.3 for pressure.

4.2.3 Results and discussion

Velocity and temperature distributions in the central plane of the wood stove are described in Figure 13, for three air operation modes. Higher velocities, in the order of 2m/s are found in the left lower section and in the central part of the stove. A 30% velocity increment is obtained in the low mode. Temperature in the primary combustor is the range between 800K and 1365K, with higher temperature reached in the low mode.
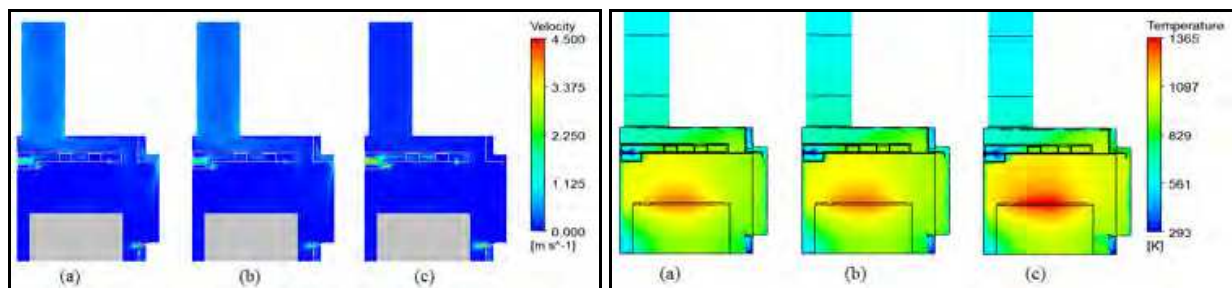

Fig. 13. Velocity and temperature distributions inside the wood stove.
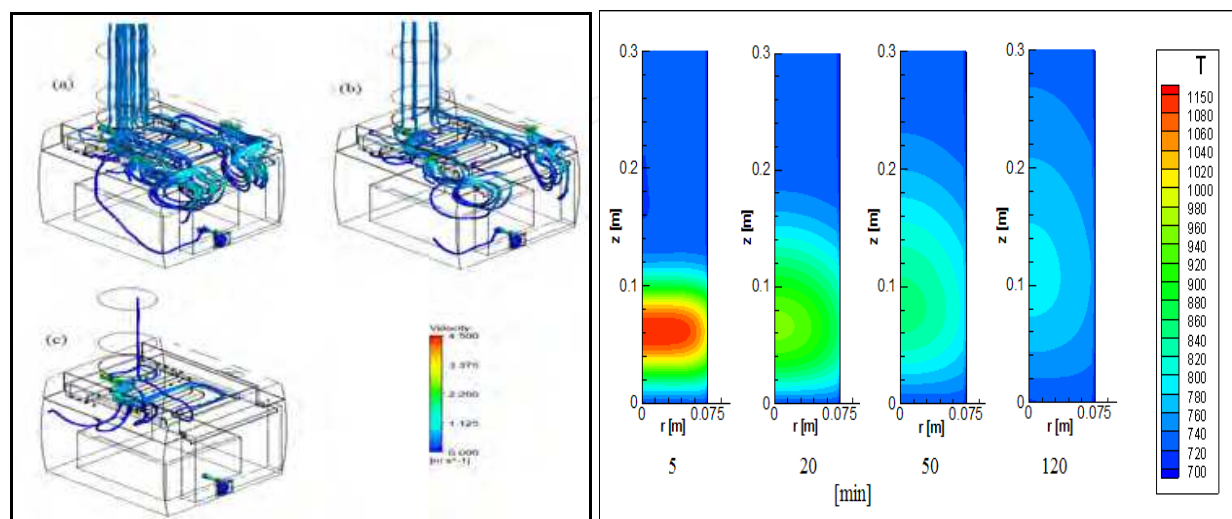

Fig. 14. Air trajectories inside the stove (at left side) and time evolution of temperature inside the porous post-combustor.

Figure 14, in the left side, depicts the air and gas trajectories in the primary combustor, where higher velocities in the range of 2.3m/s are found for the three operation modes. Time evolution for the temperature distribution in the porous post-combustor, is shown in the right hand side of Figure 13. A hot region, with temperatures in the range between 800K and 1150K can be observed to last for 5 minutes and a zone with temperatures higher than 850K can be noticed during the first 50 minutes of operation.

5. Alloy solidification and natural non-Newtonian convection predicted with a porous model

Liquid to solid phase change is a relevant process in many industrial applications, such as: polymer casting moulding, pure metals and alloys solidification, solar energy storage and food freezing and thawing. The pourpose of this section is to describe numerical solutions obtained with a porous media model and the FVM that have been applied to solidification of pure metals and alloys. The sequential solution of the discretized system of fluid mechanics and convective heat transfer is accomplished by the PSIMPLER algorithm (Moraga et al., 2010).

5.1 Physical situation and mathematical model

The physical situation related to each one of the three cases studied is shown schematically in Figure 15. The first case corresponds to the solidification of pure aluminum, and the second is the solidification of aluminum alloys with 1.7% Si. In all cases the liquid to solid phase change occurs inside a square cavity with the right vertical wall and the horizontal ones being adiabatic. The left-side wall is subjected to a convective condition, of the Robin type, for case 1, while in case 2 an imposed temperature condition is assumed, of the Dirichlet type. The fluid mechanics in the mushy zone and in the liquid phase is based on laminar flow, with a power law non-Newtonian model (n=0.5). Density is assumed to vary linearly with temperature, according to the approximation of Boussinesq. A porous medium model, with a Darcy number $Da=1.37\times10^{-5}$[26], for an average pore diameter $dm = 1.2\text{x}10^{-5}$ is proposed to describe the fluid motion in the mushy zone, along with the general Darcy-Brinkman-Forchheimer porous flow model.

Case 1 (Al); Bi = 3.3

Case 2: (Al- 1.7%Si) and $\quad h \cdot (T\big|_{x=0} - T_{\infty}) = -k \dfrac{\partial T}{\partial x}\bigg|_{x=0}$
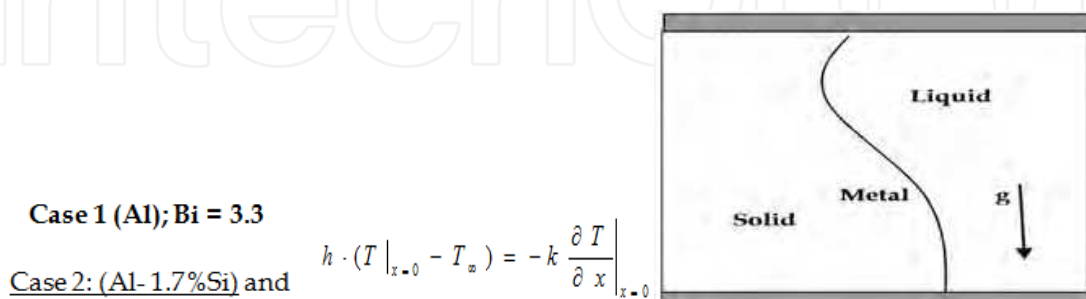
Fig. 15. Solidification of a pure metal, a binary and a terniary alloy in a square cavity.

The mathematical model includes continuity, linear momentum and energy equations in porous media

$$\frac{\partial u}{\partial x} + \frac{\partial v}{\partial y} = 0 \tag{40}$$

$$\frac{\rho}{\varepsilon}\frac{\partial u}{\partial t} + \frac{\rho}{\varepsilon^2}\left[u\frac{\partial u}{\partial x} + v\frac{\partial u}{\partial y}\right] = -\frac{\partial p}{\partial x} + \frac{\eta}{\varepsilon}\left[\frac{\partial^2 u}{\partial x^2} + \frac{\partial^2 u}{\partial y^2}\right] - \left[\frac{\eta}{K} + \frac{\rho \cdot C}{\sqrt{K}}|\vec{V}|\right]u \tag{41}$$

$$\frac{\rho}{\varepsilon}\frac{\partial v}{\partial t} + \frac{\rho}{\varepsilon^2}\left[u\frac{\partial v}{\partial x} + v\frac{\partial v}{\partial y}\right] = -\frac{\partial p}{\partial y} + \rho \cdot g \cdot \beta \cdot (T - T_C) + \frac{\eta}{\varepsilon}\left[\frac{\partial^2 v}{\partial x^2} + \frac{\partial^2 v}{\partial y^2}\right] - \left[\frac{\eta}{K} + \frac{\rho \cdot C}{\sqrt{K}}|\vec{V}|\right]v \tag{42}$$

$$\left[\rho \cdot \left[1 + \varepsilon\frac{h_{fs}}{C_p} \cdot \frac{\partial f_{PC}}{\partial T}\right] \cdot \frac{\partial T}{\partial t} + \rho \cdot \left(u\frac{\partial T}{\partial x} + v\frac{\partial T}{\partial y}\right)\right] = \frac{k}{C_p}\left[\frac{\partial^2 T}{\partial x^2} + \frac{\partial^2 T}{\partial y^2}\right] \tag{43}$$

where the liquid phase change fraction, being equal to 0 when $T < T_S$ and equal to 1 when $T > T_L$ is calculated from

$$f_{pc} = [(T - T_S)/(T_L - T_S)]^m \quad \text{for } T_S < T < T_L \tag{44}$$

The dynamic apparent viscosity is $\eta = \eta_l / f_{pc}$, for Newtonian and non-Newtonian fluids, with η_l and the deformation rate for the power law model defined as follows

$$\eta_l = \mu \cdot \dot{\gamma}^{n-1} \quad \dot{\gamma} = \left\{2 \cdot \left[\left(\frac{\partial u}{\partial x}\right)^2 + \left(\frac{\partial v}{\partial y}\right)^2\right] + \left[\frac{\partial u}{\partial y} + \frac{\partial v}{\partial x}\right]^2\right\}^{\frac{1}{2}} \tag{45}$$

5.2 Computational implementation

The mathematical models presented in the previous equations were solved with the finite volume method and the PSIMPLER algorithm developed and programmed in FORTRAN. The PSIMPLER algorithm is a mixture of two algorithms, SIMPLER and PISO (Moraga et al., 2010). In all the cases, the grid used was of the overlapping type, and 40x40, 60x60 and 80x80 grid sizes were evaluated. The results are presented for a 60x60 grid, which was efficient in time and accurate enough. The values for the under-relaxation factors used for the two velocity components, temperature and pressure were different for pure metals and for binary and ternary alloys

$$a_u = a_v = 0.2 ; a_T = 0.1 ; a_P = 0.7 \text{ (pure metal)} \quad \text{and} \quad a_u = a_v = 0.5 ; a_T = 0.3 ; a_P = 0.9 \text{ (alloys)} \tag{46}$$

The iterative procedure was finished when the difference between $\Phi^k_{i,j} - \Phi^k_{i,j}$ at two successive iterations was smaller or equal to ξ, for all control volumes and at each time step, with $\xi = 10^{-6}$ for velocity and $\xi = 10^{-3}$ for temperature.

5.3 Results and discussion

The first case describes the solidification of pure aluminum metal, with $Ra = 10^5$, by using the proposed Darcy-Brinkman-Forchheimer porous model for the mushy zone and three alternative temperature dependent liquid phase fractions, defined by changing the exponent

m in Eq. (44). Figure 16 shows that the time evolution for the temperature distributions obtained with the FVM, for $m = 0.5$, 1.0 and 2.0, in dashed lines is in agreement with the values calculated by the finite element method and the classical mathematical model, shown in continuos lines (Cruchaga et al., 2000).
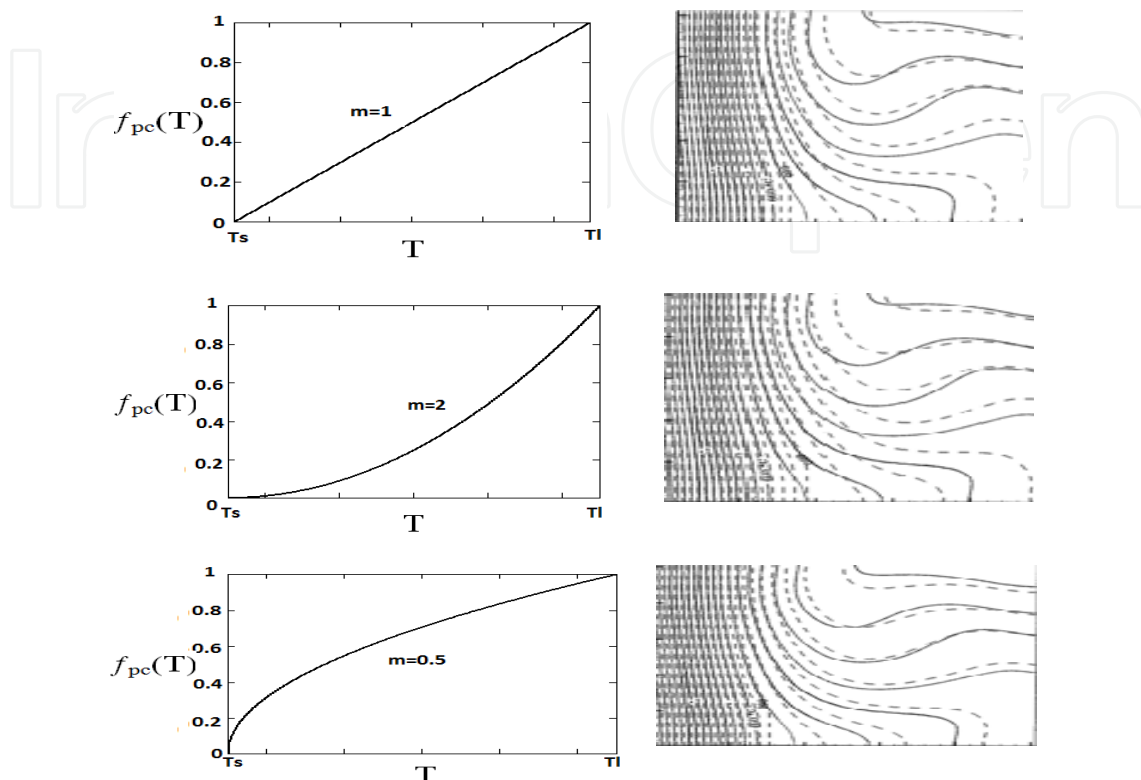

Fig. 16. Isotherms time evolution for Al solidification with Ra=10⁵, present porous model and Cruchaga et al., 2000 results.

The time evolution of the solidification front for the aluminum, calculated with the general porous media model is shown in figure 17 to be in agreement with the results obtained with the classical model.
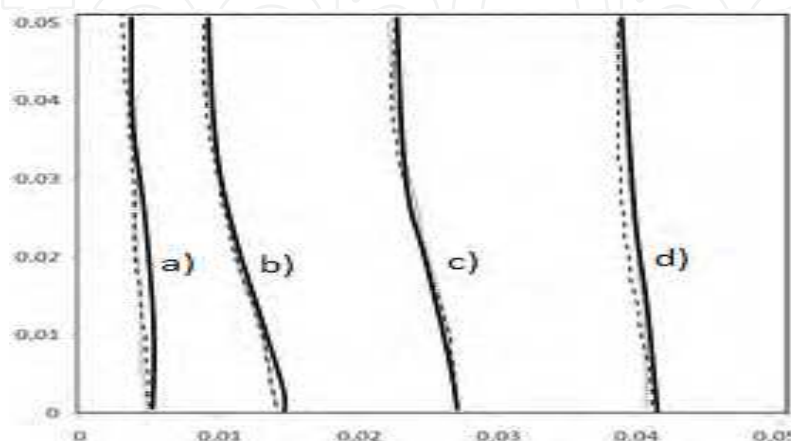

Fig. 17. Time evolution of the Al solidification front.

In case 2, the melt characterization by a non-Newtonian power law model, with a power index n = 0.5, is investigated along the use of the DBF porous model for the mushy zone, to describe the solidification of the binary Al-1.7wt%Si, when Ra=2.5x10^5. Figure 18 describes the evolution in time of the isotherms (at the left side) and of the steamlines in the liquid phase and in the mushy zone (at the rigth side), calculated with FVM by assuming either a Newtonian or a non-Newtonian power law fluid models. The pseudoplastic fluid assumption (n=0.5) originates a slighty faster convection, requiring lower time to complete the solid to liquid phase transformation.
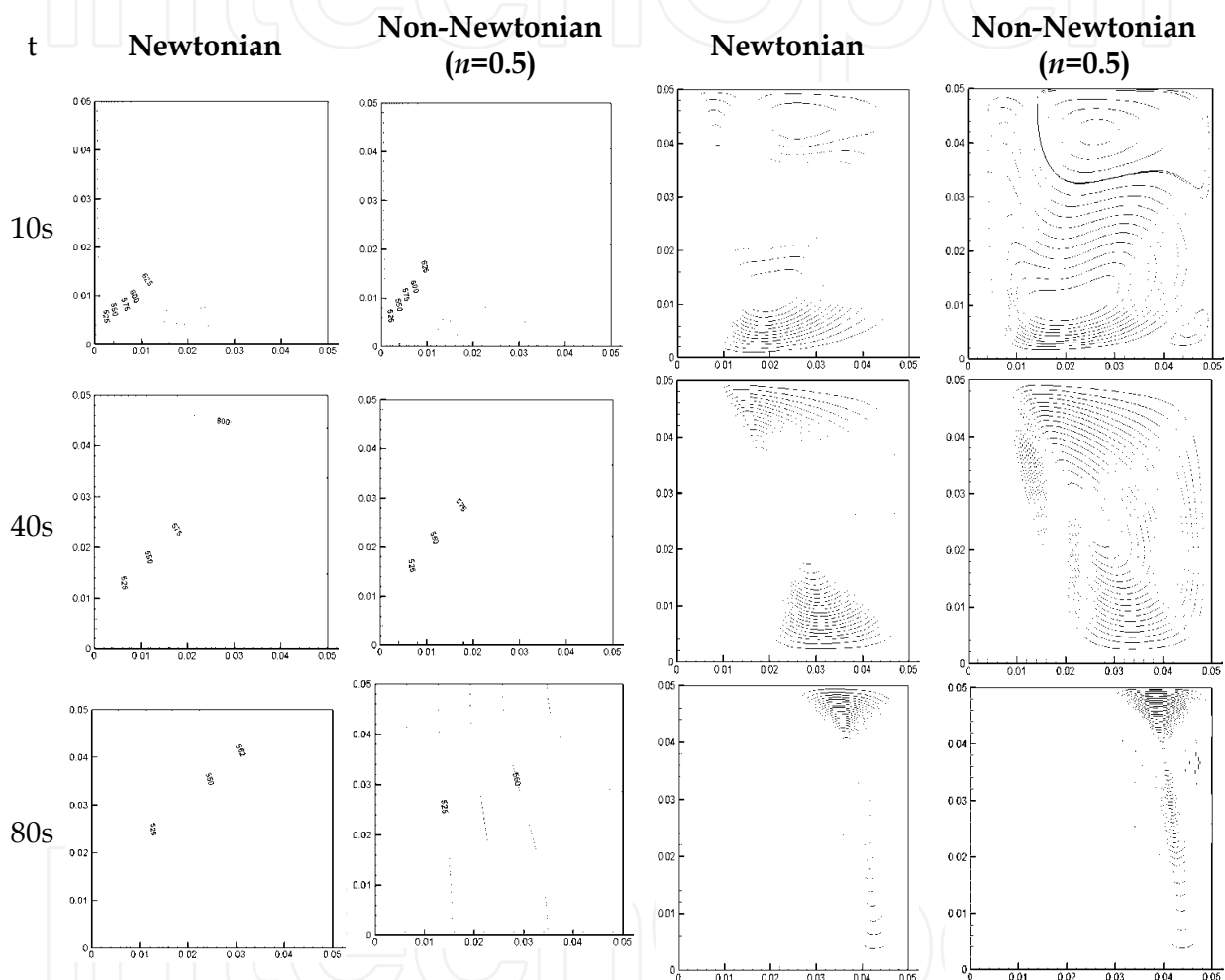

Fig. 18. Isotherms and stream function for Al-1.7%Si solidification calculated for Ra = 2.5 x 10^5.

6. Mixed turbulent convection and diffusion in a bioreactor

In the last decades, the municipal waste materials (MWM) outputs in many countries have increased significantly due to the large increase in population and industries. These wastes contain organic matter that can be recovered, and through recycling, MWM can be returned to the environment. One option in that direction, for example, is to use them as fertilizers. Another interesting possibility is to use them as fuels. In this way, in addition to solving the problem of MWM disposal, the recycling of these materials becomes a useful source of energy. For this, the MWM require usually a pre-treatment to eliminate water, in order to

have good combustion. This process is essentially a method for humidity control of the waste, which has a great impact in combustion efficiency.

The numerical modeling of heat and mass transfer involved in the drying process without self-heating has motivated several studies using finite difference methods (Kaya et al., 2006; Kaya et al., 2008, Chandra & Talukdar, 2010; Sheng et al., 2009). These studies have provided useful insight into the phenomenon, but the air flow regime in a typical drying bioreactor is nevertheless turbulent. Therefore there is interest in the analysis and characterization of this process in the fully turbulent flow regime. In this case also the self-heating of the material due to chemical and biological reactions is described.

6.1 Physical situation of an experimental bioreactor

In order to compare the model results with experimental data, we perform the computations for a case with the dimensions of the experimental bioreactor: 1 m × 1 m × 1 m, in the x, y and z coordinate directions respectively (see Fig. 19). The walls are assumed adiabatic and impermeable. Air at ambient temperature is forced into the reactor through an inflow in the plane $z = 0$. This inflow has a section of 0.05 m × 0.05 m and is located at the center of the lower wall. The air entering through this opening flows past the block of MWM inside the reactor fulfilling the drying of this material. The air outflow is located at the center of the top wall ($z = 1$ m) and has the same dimensions of the inflow located below.
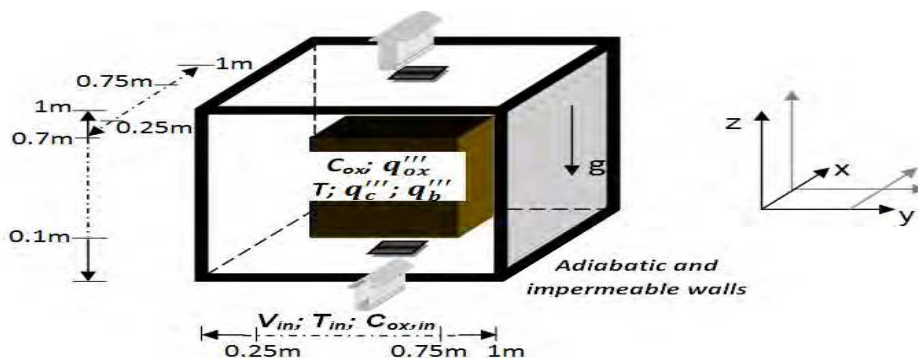

Fig. 19. 3D physical situation used for an experimental bioreactor.

The physical situation presented in this work is the same that is studied experimentally in reference (Rada et al., 2007), which provides a good source for validation of the general mathematical modeling.

6.2 Mathematical model for the bioreactor

The κ-ε turbulence model, equations (28) to (35), is used for the modeling of air flow within the reactor (Launder & Spalding, 1974), coupled with a diffusion model proposed by Sidhu et al. (Sidhu et al., 2007), and presented in equations (11) to (15).

The air flow inside the reactor is governed by continuity and by the Navier-Stokes equations.

The initial velocity is taken as zero: $\vec{v}(x,y,z,0) = 0$. The prescribed value for the inlet velocity is 1m/s in the z coordinate:

$$u_{in}(x,y,0,t) = 0 \; ; \; v_{in}(x,y,0,t) = 0 \; ; \; w_{in}(x,y,0,t) = 1 m / s \qquad (47)$$

At the outlet, zero-gradient outflow boundary conditions are applied. The walls are considered adiabatic and impermeable. The temperature of the air at the inlet is constant and an initial linear distribution in the domain was assumed:

$$T(x,y,0,t) = 283 \; K \; ; \qquad T(x,y,z,0) = 283 - \frac{z}{0.2} \qquad (48)$$

Inside the MWM the process is considered essentially as diffusion in porous medium, and therefore the velocities are zero in the region occupied by the block of material. Constant oxygen concentration is imposed around the MWM volume,

$$C_{ox}(x,y,z,t) = 0.272 \; kg / m3 \left[for(x,y,z) \; outside \; the \; MWM \right] \qquad (49)$$

The initial temperature and oxygen concentration within the MWM are considered homogeneous,

$$T(x_{wm},y_{wm},z_{wm},0) = 283 \; K \; ; \; C_{ox}(x_{wm},y_{wm},z_{wm},0) = 0.272 \; kg / m^3 \qquad (50)$$

6.3 Numerical simulation with finite volume method

The sequential coupling of these main variables (external iterations) is done with the SIMPLE method. Under-relaxation is applied during these external iterations, with a relaxation coefficient of 0.5 for all the variables, except for the pressure correction for which a value of 0.8 was used instead.

The bioreactor was discretized with a non-uniform mesh of 32×62×82 finite volumes in x, y and z directions, respectively. Additionally, a buffer zone extending for 1 m beyond the exit of the reactor is considered, in order to ensure a zero-gradient condition at the outlet of the computational domain. The waste material occupies a volume inside the reactor equivalent to a parallelepiped with dimensions of 0.5×0.5×0.6 m³. The discretization of this sub-region of the domain comprises 16×40×40 finite volumes in the x, y and z directions, respectively. The simulation was carried out for a total time of 696 hr. The time step was 3600 s for most of this period. During the first hour a dynamic time step was used (starting with a step of 0.001 s) in order to achieve convergence at each time step during the initial fast transient period starting from the prescribed initial condition.

6.4 Comparison with experimental data

In the experimental bio-drying reactor analyzed in reference (Rada et al, 2007), three thermocouples were installed inside the MWM, along the z direction, at equal intervals of 0.2 m in z direction inside of MWM, to measure the internal temperature in the material. Figure 20 presents the numerical results of temperature evolution obtained with the mathematical model and the numerical simulation described in previous sections. The numerical results in Fig. 20 were obtained in the following three (x, y, z) positions: P1(0.49,0.44,0.19), P2(0.49,0.44,0.39) and P3(0.49,0.44,0.59). The values for all coordinates are

in meters. The results for the time evolution of the temperature in Fig. 20 are consistent with the behavior showed by Rada et al. (2007). The self-heating, product of the biological and chemical heat generation is clearly observable. Initially, a sudden increase of temperature occurs in the three sampled positions until 90 h. For all times, the temperature at point P2 is greater than the others. This can be attributed to its more inner position, making more difficult for the locally generated heat to diffuse to the surface, where is removed by the flowing air. Points P1 and P3, being located nearer to the surface, can release more easily the generated heat to the surrounding air. The asymmetry in the temperature at P1 and P3 is due to the location of P1 on the side subjected directly to the impinging flow of cold air.

After about 96 h, the temperatures at the three points moderate their rate of increase, and the maximum temperatures occur at about t = 168 h for all these positions. The maximum temperature reached inside the MWM is close to 340 K, at the central position P2. The existence of these maxima can be associated with an intrinsic self-moderation of the rate of heat generation, given by the last term in Eq. (11). That term, describing the heat released by the biological activity of micro-organisms initially increases with the temperature, as their population grows, but after exceeding 318 K approximately this source of heat starts to decrease, because of the progressive inhibition in micro-organism growth as the temperature continues to increase. After 168 h, the temperature decreases in all positions as the internal heat source has become weaker and at the same time a heat diffusion pattern inside the material has established, allowing and effective removal of the generated heat towards the surrounding air.

The table 4 shows a comparison between computed temperatures at the sampled points and experimental data from Ref. (Rada et al., 2007) at corresponding positions. The temperatures calculated in the present study approximate very well the experimental values in the three compared positions. A maximum difference of 5 K can be observed at 360 h in the position P3.

Time, h	Temperature, K					
	Thermocouple 2, Ref. [3].	P1	Thermocouple 3, Ref. [3].	P2	Thermocouple 4, Ref. [3].	P3
96	317	315	335	337	330	329
168	323	325	335	338	335	334
360	307	307	331	329	312	317
696	290	291	298	299	292	293

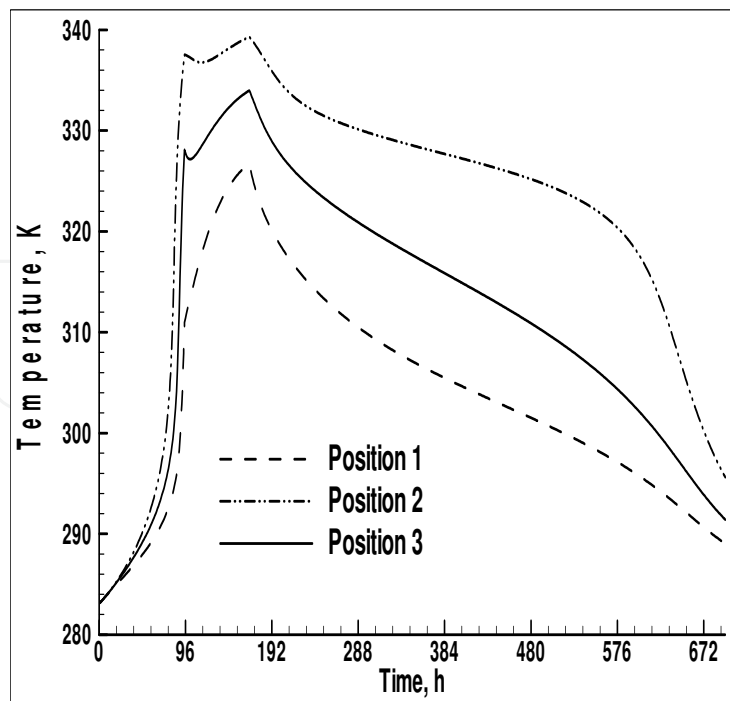Table 4. Comparison of temperatures between experimental data and calculated values.

Fig. 20. Temperature evolution in three positions of the MWM.

7. Conclusions

The FVM capabilities to produce efficient and accurate prediction of fluid mechanics, heat and mass transfer in porous media, including biological and chemical reactions or liquid to solid phase transformations, have been shown by solving four practical examples. In the first case, auto-ignition of compost piles was studied and field experimental data were used to assess the quality of FVM results for the evolution of temperature and oxygen concentration distributions. The conclusion found for this case was that a pile heigth equal to 1.7m is a critical value to produce self-ignition. Combustion in porous media, predicted by FVM, allows to conclude in the second case, that improvements on thermal energy efficiency and pollution reduction in a methane porous combustor and in a wood stove, can be achieved. The use of the FVM and a generalized DBF flow porous media model for the mushy zone was found to describe convective cooling during solidification of non-Newtonian melted binary alloys in the third case. A conclusion found for this type of phase change processes was that the CPU time requiered for the numerical simulation can be reduced one order of magnitude by using a new improved predictor-corrector sequential algorithm, PSIMPLER, for the pressure-velocity-temperature-concentration calculation procedure. In the fourth case, the FVM along the k-ε turbulence model, were used to describe 3D turbulent convective heat transfer, with self heating of the porous media due to chemical and biological reactions, in a bioreactor. The conclusions found in this case were that the FVM simulations for the dependent variables were successfully validated with experimental values and that the effects of reactor geometry, self-heating parameters, air flow and temperature in the bioreactor perfomance can be evaluated. Finally, it is concluded that the use of FVM and adequate mathematical models along to experimental physical results can be used to investigate physical, biological and chemical coupled problems in order to achieve improved thermal efficiency, adequate use of energy resources and pollution reduction in these processes.

8. Acknowledgements

9. References

Chandra, V.P. & Talukdar, P. (2010). Three dimensional numerical modeling of simultaneous heat and moisture transfer in a moist object subjected to convective drying. *International Journal of Heat and Mass Transfer*, Vol.53, pp.4638–4650, ISSN 0017-9310.

Chen, X.D. & Mitchell D.A. (1996). Star-up strategize of self-heating and efficient growth in stirred bioreactor for solid state bioreactors, *Proceedings of the 24th Annual Australian and New Zealand Chemical Engineering Conference (CHEMECA 96)*, pp.111-116, ISSN 0858256584.

Cruchaga, M. & Celentano, D. (2000). A Finite Element Thermally Coupled Flow Formulation for Phase-Change Problems, *Int. J. Numer. Meth. Fluids*, Vol. 34, pp. 279-305.

Ferziger, J. H. & Peric, M. (2002). Computational Methods for Fluid Dynamics, Springer, Berlin, ISBN 3540594345.

Foutko, S.I.; Shanbunya, S.I. & Zhdnadok, S.A. (1996). Superadiabatic combustion wave in a diluted methane-air mixture under filtration in a packed bed, in: *Proceedings of the 26th International Symposium on Combustion/The Combustion Institute*, Mink, Belarus.

Jin-Sheng Leu; Jiin-Yuh Jang & Wen-Cheng Chou. (2009). Convection heat and mass transfer along a vertical heated plate with film evaporation in a non-Darcian porous medium. *International Journal of Heat and Mass Transfer*, Vol.52, Vol.5447–5450, ISSN 0017-9310.

Kaya, A.; Aydın, O. & Dincer, I. (2006). Numerical modeling of heat and mass transfer during forced convection drying of rectangular moist objects, *International Journal of Heat and Mass Transfer*, Vol.49, pp.3094–3103, ISSN 0017-9310.

Kaya, A.; Aydin, O. & Dincer, I. (2008). Heat and mass transfer modeling of recirculating flows during air drying of moist objects for various dryer configurations. *Numerical Heat Transfer; Part A: Applications*, Vol.53, No.1, pp. 18-34, ISSN 1521-0634.

Launder, B.E. & Spalding, D.B. (1974). The numerical computation of turbulence flow. *Computer Methods in Applied Mechanics and Engineering*, Vol.3, pp.269-289, ISSN 0045-7825.

Moraga, N., Zambra, C. (2008). Autoignición 3D en depósitos de lodos provenientes de tratamientos de aguas residuales. INGENIARE, Revista Chilena de Ingeniería, Vol.9, No.3, pp. 352-357, ISSN: 0718-3291.

Moraga, N.O.; Andrade, M.A. & Vasco, D. (2010). Unsteady mixed convection phase change of a power law non-Newtonian fluid in a square cavity. *International Journal of Heat and Mass Transfer*, Vol.53, pp.3308-3318, ISSN 0017-9310.

Moraga, N.O.; Corvalán, F.; Escudey, M.; Arias, A. & Zambra, C.E. (2009). Unsteady 2D Coupled Heat and Mass Transfer in Porous Media With Biological and Chemical Heat Generations. *International Journal of Heat and Mass Transfer,* Vol.52, pp.25-26, ISSN 0017-9310.

Moraga, N.O.; Ramírez, S.C. & Godoy, M.. (2010). Study of convective Non-Newtonian alloy solidification in moulds by the PSIMPLER/ Finite Volume Method. *Numerical Heat Transfer,* Vol.57, pp.936-953, ISSN 1521-0634.

Moraga, N.O.; Rosas, C.E.; Bubnovich, V.I. & Tobar J. (2008). On predicting two-dimensional heat transfer in a cylindrical porous combustor. *International Journal of Heat and Mass Transfer*, Vol.51, pp.302-311, ISSN 0017-9310.

Moraga, N.O.; Sánchez, G.C. & Riquelme, J.A.. (2010). Unsteady mixed convection in a vented enclosure partially filled with two non-Darcian porous layers. *Numerical Heat Transfer, Part A*, Vol.57, pp.1-23, ISSN 1521-0634.

Moraga, N.O. & Lemus-Mondaca, R. (2011). Numerical conjugate air mixed convection/non-Newtonian liquid solidification for various cavity configurations and rheological models". *International Journal of Heat and Mass Transfer,* Vol. 54, (23), pp. 5116-5125.

Nield, D. &. Bejan, A. (1992). Convection in Porous Media, Springer-Verlag, New York, ISBN 0387984437.

Patankar, S. (1980). Numerical Heat Transfer and Fluid Flow, Hemisphere, Washington, ISBN 0891165223.

Rada, E.C.; Taiss, M.; Ragazzi, M.; Panaitescu, V. & Apostol, T. (2007). Lower heating value dynamics during municipal solid waste bio-drying, *Environmental Technology*, Vol.28, No.4, pp.463-469, ISSN 0959-3330.

Richards, L.A. (1931). Capillary Conduction of Liquids Through Porous Mediums. *Journal of Applied Physics*, Vol.1, pp. 318-333, ISSN 0021-8979.

Serrano, S. (2004). Modeling Infiltration with Approximated Solution to Richards Equation. Journal of Hydrologic Engineering, Vol.9, No.5, pp. 421-432, ISSN 1084-0699.

Sidhu, H.S.; Nelson, M.I. & Chen, X.D. (2007). A simple spatial model for self-heating compost piles. *ANZIAM J. (CTAC2006)*, Vol.41, pp.C135-C150, ISSN 1446-8735.

Versteeg, H.K. & Malalasekera, W.. (1995). An Introduction to Computational Fluid Dynamics. The Finite Volume Method. John Wiley & Sons, (Ed. 1), New York, ISBN 0-47023515-2.

Zambra, C.E.; Moraga, N.O. & Escudey, M. (2011). Heat and Mass Transfer in Unsaturated Porous Media: Moisture Effects in Compost Piles Self-Heating. *International Journal of Heat and Mass Transfer,* Vol.54, pp.2801-2810, ISSN 0017-9310.

Zambra, C.E.; Rosales, C.; Moraga & N.; Ragazzi, M. (2011). Self-Heating in a bioreactor: Coupling of heat and mass transfer with turbulent convection. International Journal of Heat and Mass Transfer, Vol.54, pp.5077-5086, ISSN 0017-9310.

Zhdanok, S.A.; Kennedy, L.A. & Koester, G. (1995). Superadiabatic combustion of methane-air mixtures under filtration ina a packed bed. *Combustion and Flame*, Vol. 100, pp.221-131.
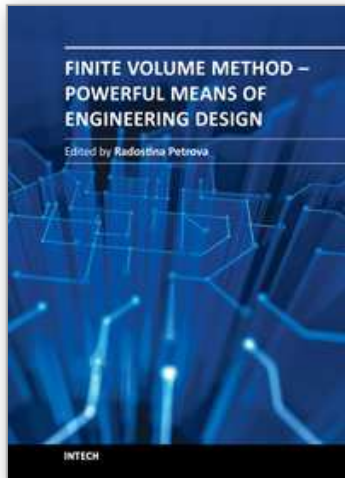
Finite Volume Method - Powerful Means of Engineering Design

Edited by PhD. Radostina Petrova

ISBN 978-953-51-0445-2

Hard cover, 370 pages

Publisher InTech

Published online 28, March, 2012

Published in print edition March, 2012

We hope that among these chapters you will find a topic which will raise your interest and engage you to further investigate a problem and build on the presented work. This book could serve either as a textbook or as a practical guide. It includes a wide variety of concepts in FVM, result of the efforts of scientists from all over the world. However, just to help you, all book chapters are systemized in three general groups: New techniques and algorithms in FVM; Solution of particular problems through FVM and Application of FVM in medicine and engineering. This book is for everyone who wants to grow, to improve and to investigate.

How to reference

In order to correctly reference this scholarly work, feel free to copy and paste the following:

Nelson O. Moraga and Carlos E. Zambra (2012). On FVM Transport Phenomena Prediction in Porous Media with Chemical/Biological Reactions or Solid-Liquid Phase Change, Finite Volume Method - Powerful Means of Engineering Design, PhD. Radostina Petrova (Ed.), ISBN: 978-953-51-0445-2, InTech, Available from: http://www.intechopen.com/books/finite-volume-method-powerful-means-of-engineering-design/on-fvm-transport-phenomena-prediction-in-porous-media-with-chemical-biological-reactions-or-solid-li